An analytical model for the loading capacity of splice-retrofitted slender timber columns

Citation for published version:
Li, H, Qiu, H & Lu, Y 2020, 'An analytical model for the loading capacity of splice-retrofitted slender timber columns', *Engineering Structures*, vol. 225, 111274. https://doi.org/10.1016/j.engstruct.2020.111274

Digital Object Identifier (DOI):
10.1016/j.engstruct.2020.111274

Published In:
Engineering Structures

An analytical model for the loading capacity of splice-retrofitted slender timber columns

Hongmin Li[a*] , Hongxing Qiu[b], Yong Lu[c]

[a] Department of Timber Structures, College of Materials Science and Engineering, Nanjing Forestry University, 159 Longpan Road, Nanjing, 210037,China

[b] Key Laboratory of Concrete and Prestressed Concrete Structures of Ministry of Education, Southeast University, Nanjing 210096, China

[c] Institute for Infrastructure and Environment, School of Engineering, University of Edinburgh, Edinburgh EH9 3JL, UK

Abstract: Retrofitting timber columns in traditional timber structures with a steel jacketed splice joint has advantages of aesthetic appearance and similar mechanic performance to the intact columns as compared to conventional simple splice columns. The axial compression behavior of such retrofitted splice columns has been studied experimentally in detail. However, there is still a lack of a calculation model for their axial compressive strength and general guideline for their design. The objective of this study is to establish a theoretical calculation model for this type of retrofitted splice columns. Firstly, a theoretical model for the axial compressive strength of splice columns retrofitted with a steel jacket is proposed considering the contact stresses at a splice joint and the relevant stability theory. Secondly, the buckling modes of splice columns and the actual stress distributions at the splice joints (i.e. the compressive stresses at the steel-timber and timber-timber interfaces) are thoroughly investigated. Finally, the theoretical model is validated by the experimental data and finite element analysis results with different splice parameters. Comparisons show that the theoretical calculations in terms of the bearing capacity and stability coefficient agree

* Corresponding author. Tel.:+86 15251857592

E-mail address: lihongmin@njfu.edu.cn (Hongmin Li)

well with the experimental results. The proposed theoretical model is also shown to be suitable for predicting the axial compressive strength of a retrofitted splice column with the location of the splice from the column end ranging from 1/5 to 1/2 of the column length. The relative errors in the theoretical bearing capacities with respect to the finite element results are found to be less than that using the stability coefficient. From the analysis results, the length of the splice and the total length of the steel jacket are recommended to be in the range of 0.5~1.5 and 2~4.5 times of the column diameter, respectively. This proposed theoretical model can be applied in the retrofitting design of timber columns in historical timber structures, and it can also be applied in the development of new large-space timber structures where splice columns may be incorporated.

Keywords: Splice column, Steel jacket, Stable bearing capacity, axial compression

1. Introduction

Decaying and aging are common in timber elements in historical timber structures. Considering the conservation of the original material and structural appearance, it is preferable to replace only the severely decayed part with a new segment through a splice joint. The flexural performances of different types of splice joints in retrofitting timber beams, such as a lapped scarf joint, dowel-type timber connections, glued-in rods timber connection, self-tapping screws, and long treaded rods have been investigated by many researchers [1-13]. However, there have been limited studies on the axial compressive performance of the spliced columns.

Some existing studies concerning the compression behavior of spliced columns have mainly focused on spliced short columns through experimental investigations [14, 15]. However, slender timber columns are common in ancient timber structures, and such slender columns are usually under both axial load and bending. Thus, the failure of a splice column depends very much on the stable bearing capacity. For intact timber columns under bending and compression, analytical methods are available for the calculation of the load bearing capacity. Buchanan [16] proposed a strength model with bending and axial load interaction for intact timber members. Huang et al. [17] proposed an analytical model to evaluate the load-carrying capacity of slender engineered bamboo/wood columns subjected to biaxial bending and compression. Song and Lam [18] proposed a numerical analysis model based on the column deflection curve method and verified by the material test and biaxial eccentric compression test of timber beam-columns. However, there is a lack of theoretical calculation models and design guidelines for retrofitting the timber columns, and no information is available with regard to the effect of the length and position of the splices.

In this paper, an analytical model for the axial compression capacity of the splice-retrofitted columns using a steel jacket is developed. This type of splice joint reinforced by a steel jacket has been proposed in recent studies and the axial compressive performance of columns retrofitted with this type of splice has been investigated experimentally [19, 20]. The steel jacket is used to enhance the wood joint through confinement and friction between the wood joint and the steel jacket, thus increasing the moment transfer capacity of the joint. However, there has not been a simplified theoretical model which may be used in the design analysis of the load bearing capacity of timber columns retrofitted with this type of splice joint. In the present paper, an analytical model for the axial compression capacity of the splice-retrofitted columns using the steel jacket is proposed, based on the results from the experiment and the stability theory. Furthermore, a finite element simulation study is performed to examine the influence of the main parameters on the behavior of the splice joint.

2. Experimental programme

The axial compressive performance of the splice columns retrofitted with the steel jacket has been analysed in detail in the earlier experimental study [19, 20]. Herein the key design parameters for the splice joint, material properties, and the main experimental conclusions of the retrofitted spliced columns are briefly introduced. The information will provide a basis for the development of the theoretical calculation model and the numerical analysis.

2.1. Design of test specimens

The detailed configurations of the column specimens are illustrated in Fig 1. The traditional half-cut joint was adopted for the splice and the joint was located at the mid-height of the columns. L_s and L_t are the length of the steel jacket and the splice length, respectively. $L_e = (L_s - L_t)/2$ is the length of the steel jacket extending from the splice faces. The length and the nominal diameter of the columns were 1800mm and 100mm, respectively. A total of 15 column specimens were tested, including two groups and six test column series, namely a) intact columns as the reference for jointed columns (referred to as group RC); b) jointed columns reinforced by steel jacket (referred to as group SC), and this group was further divided into 5 series, with SC1 and SC3 focusing on the influence of L_e and SC2, SC4, and SC5 focusing on the influence of L_t. The details of the 15 tested columns are summarised in Table 1.

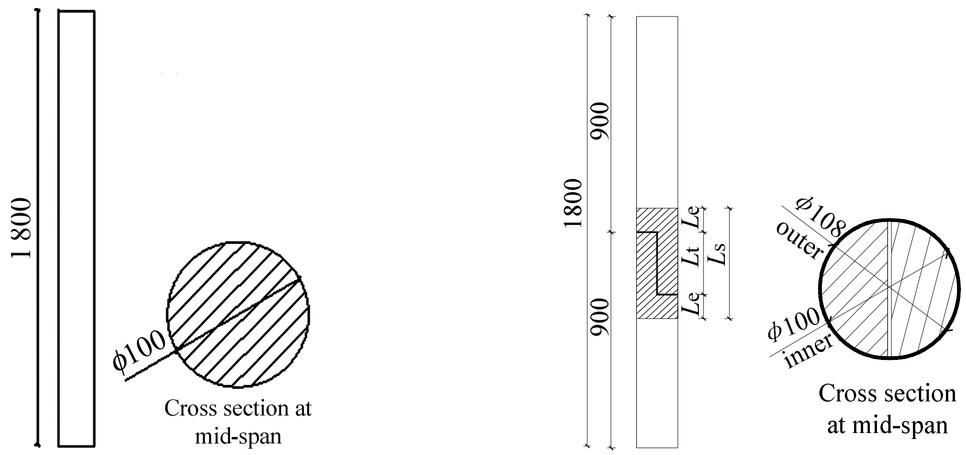

(a) (b)

Fig. 1. Test timber columns: (a) Intact columns (RC); (b) Splice columns (SC)

Table 1 Details of the 15 specimens

Column group	Column series	Number of specimens	L_t (mm)	L_e (mm)
RC	RC	5	—	—
	SC1	2	130	50
	SC2	2	130	100
SC	SC3	2	130	150
	SC4	2	50	100
	SC5	2	200	100

2.2. Material properties and test method

The mechanical properties of the timber materials for each specimen were experimentally determined [21-23] and the results are listed in Table 2, in which f_c, E, f_m, $f_{c,R}$ and $f'_{c,R}$ denotes respectively the compressive strength along the wood grain, compressive modulus of elasticity along the wood grain, bending strength, overall compressive strength in the radial direction and local compressive strength in the radial direction. The average bending strength is 86.5 MPa and it has the least coefficient of variation (COV). There are interactions among parameters, e.g. the average value and coefficient of variation of the ratio of the E to f_c is 315.8 and 8.0%, respectively. The average value and coefficient of variation of the ratio of the f_m to f_c is 2.77 and 13.8%, respectively.

The modulus of elasticity and tensile strength of the steel jackets were found to be 208 GPa and 340.2 MPa, respectively [24]. Since the inner diameter of the steel jacket was the same as the diameter of the column in the design, no interface pressure was considered in the steel jacket.

Table 2 Material properties of column specimens

Column	f_c/MPa	E/MPa	f_m/MPa	$f_{c,R}$/MPa	$f'_{c,R}$/MPa
RC-1	27.1	9110	-	-	-
RC-2	32.3	9650	83	2.66	3.49
RC-3	38.8	11288	93	3.00	3.11
RC-4	30.1	9824	93	1.68	3.15

RC-5	33.2	10335	89	2.59	-
SC1-1	29.1	9229	76	2.18	3.19
SC1-2	32.9	11844	78	2.77	4.36
SC2-1	28.5	8573	71	2.35	4.04
SC2-2	40.2	10911	91	3.76	-
SC3-1	31.3	10928	97	2.05	4.49
SC3-2	26.9	8711	97	-	3.96
SC4-1	33.7	9396	88	3.2	-
SC4-2	27.6	8121	94	2.06	3.36
SC5-1	26.2	8867	73	1.20	-
SC5-2	31.0	10539	88	-	-
Mean	31.3	9821.7	86.5	2.46	3.68
Cov. (%)	12.8%	10.9%	9.8%	27.0%	13.8%

The column specimens were tested under axial compression which was applied using a MTS testing machine. The columns were connected at each end to a spherical hinge (pinned end), which was then attached to a support base at the bottom and the loading head at the top. The lateral deflection was measured from a combination of two horizontal displacement transducers installed at the mid-span and arranged at a 90° angle to each other, as shown in Fig. 2.

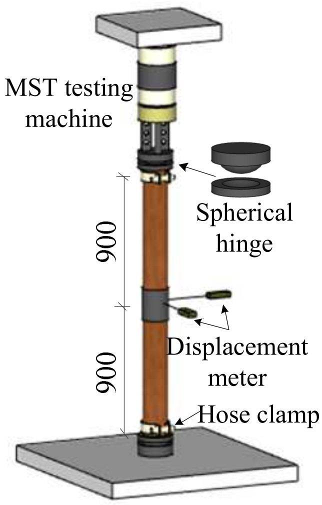

Fig. 2 Experimental set-up (Unit: mm)

2.3. Discussion of the test results

Specimens in Group RC exhibited small lateral deflection in the mid-span before the peak loads were reached. Beyond the peak loads, the lateral deflection increased abruptly, showing a characteristic of instability failure (Fig. 3a). The results from Group SC showed a decreased lateral displacement at the peak load with increased splice extension length L_e (Fig. 1), and this indicated that the stiffness of the spliced columns increased as L_e increased. It is noted that specimen SC1-1 had apparent initial bending. The initial bending led to a large lateral deflection before the ultimate load was reached and a final eccentric compression failure. For specimen CS3-2, the two splice parts wrapped in the steel jacket did not come into contact with each other at the beginning of the test, and this meant the actual length of CS3-2 was shorter than other specimens.

(a) (b)

Fig. 3. Failure modes: (a) RC, (b) SC

The ultimate axial load capacity of specimens in Group SC reached more than 50% of that of the reference Group RC (Table 3). The ultimate axial load capacity of the columns within Group SC increased as L_e increased (SC1~SC3). On the other hand, no clear trend was observed in the relation between the ultimate axial load capacity and the main splice length L_t (SC2, SC4, and SC5).

Table 3 Ultimate load of columns (kN)

Colum	RC-1	RC-2	RC-3	RC-4	RC-5	SC1-1	SC1-2	SC1-2
Ultimate load	178	186.3	239.9	203.4	203.2	69.1	130	113.8
Colum	SC2-2	SC3-1	SC3-2	SC4-1	SC4-2	SC5-1	SC5-2	
Ultimate load	203.9	164.9	177.3	138.2	90.1	101.2	130.8	

Fig. 4 summarizes the principal bending directions of the specimens in Group SC, namely, type I and type II, which are perpendicular to the splice face, and type III, which is parallel to the splice face. The actual bending direction at the failure of an individual specimen was inclined towards type III, i.e., either dominated by this mode or had a significant bending component in this direction.

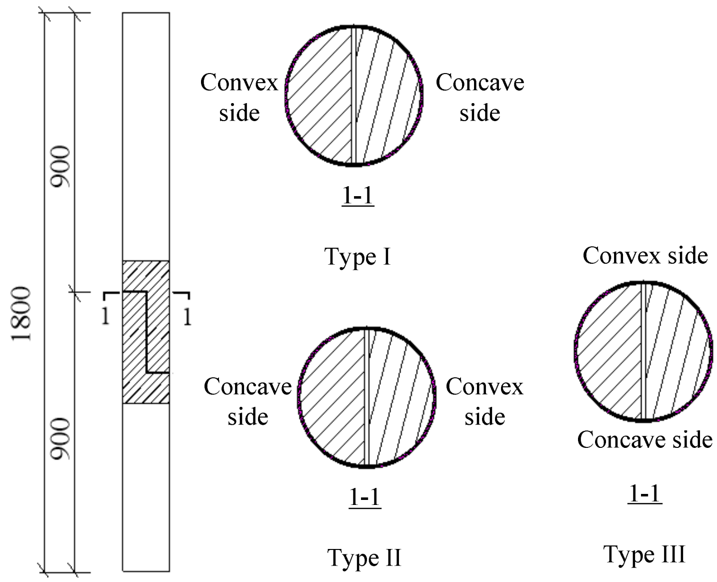

Fig. 4. Type of buckling sections for splice columns

3. Theoretical analysis

3.1. Mechanism of splice joint

As demonstrated from the test results, a certain amount of extrusion took place between the timber joint and steel jacket bearing the axial load and the moment ($P \times$ lateral deflection) at the mid-height of the retrofitted specimens. The extrusion mainly located in the upper edge of the steel jacket at the concave side and the steel jacket near mid-span of the column in the convex side of lateral deformation. There was compressive (normal) stress pointing to the column axis on the cylindrical arc surface in the concave side and the convex side. Furthermore, friction should be considered when the contact surfaces between the timber joint and steel jacket experienced a sliding. The direction of the friction was opposite to the impending sliding direction. Thus, an additional bending moment of the spliced joint was provided by the timber tendon of the joint and the steel jacket through extrusion and friction. The extrusion and friction increased with the lateral deflection. After the timber on the concave side yielded, the lateral deflection rapidly increased, leading to a marked decrease in the axial load.

3.2. Basic assumptions

A theoretical model to calculate the bending capacity of the spliced column with the steel jacket is proposed herein. In accordance with the experimental observations, the following basic assumptions are adopted:

(1) The main direction of the deflection of the splice column is assumed to be parallel to the splice face (type-III). This is consistent with the main experimental observations and will be further discussed in the finite element simulation section later.

(2) The constitutive relations of wood under compression in both longitudinal and transverse directions follow a simplified bi-linear model.

(3) For each side of the splice joint, a continuous half tenon is involved in carrying the bending moment and compression force.

(4) The extrusion stress is linearly related to the extrusion deformation, and the resultant force of extrusion stress is located at the centroid of the normal stress block.

3.3. Calculation model of bending capacity

3.3.1. Moment equilibrium

As observed from the experiment, the failure of the spliced columns mostly happened at the splice section of the joint. This failure section is taken as the free body to calculate the bearing capacity. The simplified stress diagram for this free body is shown in Fig. 5. The steel jacket at the convex and concave sides of lateral deflection is under tensile and compressive force in the longitudinal direction, respectively, as shown in Fig. 5b. Friction caused by the extrusion force is located at the inner surface of the steel jacket. The overall force diagram is shown in Fig. 5c, where σ_a is the maximum contact stress between the splice column and the edge of the steel jacket on the concave side; F_t is the component along the lateral deflection direction of the contact force at the timber column at the convex side (horizontally to the left in the schematic diagram); f_a is the friction generated by the extrusion of the steel jacket at the concave side and is perpendicular to the upper splicing surface; σ_t is the maximum contact stress of the timber column at convex side; f_t is the friction generated by the extrusion of the steel jacket at the concave side and is perpendicular to the upper splicing section; M is the bending moment at the middle section of the column with initial bending (caused by initial defects) under the peak load (N= peak load P); M_1 is the bending moment at the middle section of the column induced by the wooden tenon at upper splice section, and l is the length of the spliced column.

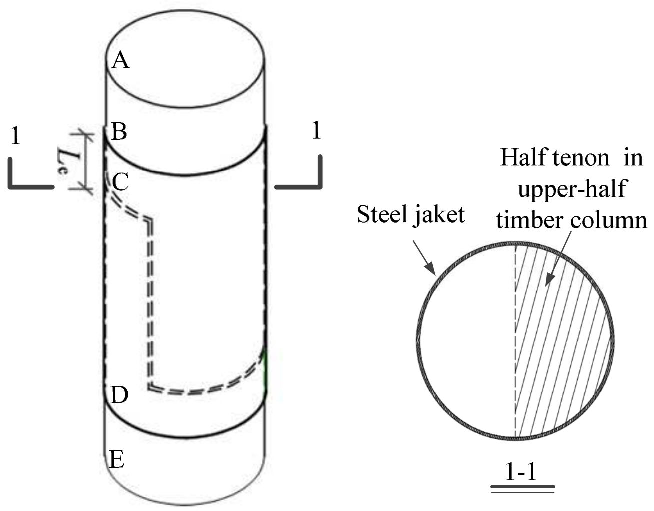

(a)

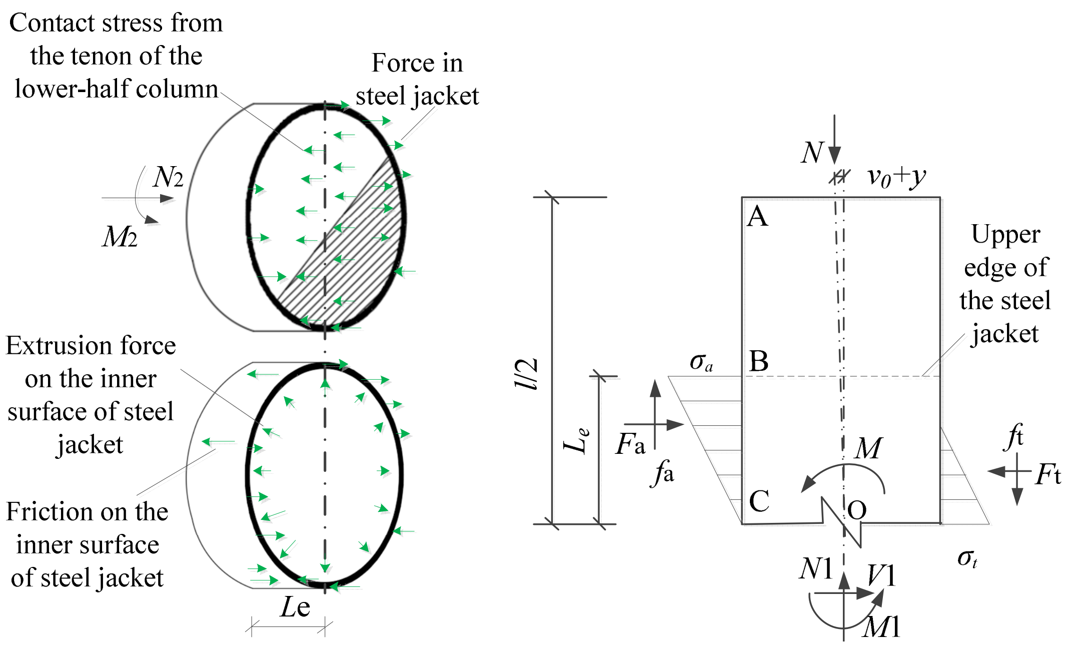

(b) (c)

Fig. 5. Free body diagrams under peak load: (a) Diagram of the joint and 1-1 section; (b) Diagram of forces in steel jacket; (c) Overall diagram of forces in upper-half timber column from 1-1 section

The condition of moment equilibrium on the center *O* of the splice surface along the lateral deformation direction can be expressed as follows:

$$M=M_1+M_s \tag{1}$$

$$M_s=M_{sa}-M_{st}+M_{saf}+M_{stf} \tag{2}$$

where M_s denotes the resistance of moment provided by the steel jacket; M_{sa} and M_{st} denote the moment generated by the contact pressure (F_a and F_t) at the concave and convex sides of the steel jacket, respectively; M_{saf} and M_{stf} denote the moment generated by the friction (f_a and f_t) at the concave and convex sides of steel jacket, respectively.

3.3.2. Axial compressive capacity

The moment at the middle section of the column with initial bending (caused by initial imperfections) under the peak load, *M*, can be expressed [25]:

$$M=(y+v_0)N \tag{3}$$

where y denotes lateral deflection caused by M; v_0 denotes the initial bending (caused by the initial defects). The lateral deflection, y, of the intact column [25] is as follows:

$$y=\frac{5Ml^2}{48E_l I}=\frac{5\pi^2 M}{48N_{\mathrm{cr}}}=\frac{5\pi^2}{48}\cdot\frac{M}{N_{\mathrm{cr}}}\approx\frac{M}{N_{\mathrm{cr}}} \tag{4}$$

where E_l denotes the compressive modulus of elasticity along the wood grain; I denotes the section moment of inertia of the intact column; N_{cr} denotes the elastic critical force of the intact column calculated by the Euler's formula.

The trend of the lateral deflection of the spliced column was observed to be similar to that of the intact column in the test. Therefore, it is assumed that the lateral deflection of the spliced column in the mid-span fits Eq. (4). Eq. (3) can be rewritten by substituting Eq. (4):

$$M=\frac{v_0 N}{1-(N/N_{\mathrm{cr}})} \tag{5}$$

For the splice columns under the combined axial compressive load and bending moment, the compressive stress and bending stress can be calculated by $\sigma_{\mathrm{c}}=N/A_{\mathrm{b}}$ and $\sigma_{\mathrm{m}}=(M-M_{\mathrm{s}})/W$. According to the superposition principle, the splice joint needed to meet the following requirement:

$$\frac{N}{A_{\mathrm{b}} f_{\mathrm{c}}}+\frac{M-M_{\mathrm{s}}}{W_{\mathrm{b}} f_{\mathrm{m}}}\leq 1.0 \tag{6}$$

where A_{b} denotes the semi-circular cross-sectional area of the splice joint, i.e. 0.5 times of the whole cylindrical section; f_{c} and f_{m} denote the compressive strength along the wood grain and bending strength, respectively; W_{b} denotes the flexural section modulus of the semi-circular tenon. The calculation of the W_{b} depends on the direction of the mid-span deflection, such as $W_{\mathrm{b}}=\pi D^3/64$ in type III of buckling sections for spliced columns. It can be calculated using the parallel shift axis formula of the rotating shaft for the type I and type II if needed.

The elastic critical force of the intact column is calculated by Euler's formula as follows:

$$N_{\mathrm{cr}} = \frac{\pi^2 E_l A}{\lambda_0^{\ 2}} \tag{7}$$

where λ_0 denotes the nominal slenderness ratio of the splice columns and the calculation is the same as the intact column.

Using Eqs. (1)-(7), it is possible to calculate the axial compressive strength of the splice column as follows:

$$N = \frac{M_{\mathrm{s}} + W_{\mathrm{b}} f_{\mathrm{m}} + (W_{\mathrm{b}} f_{\mathrm{m}} a + v_0) N_{\mathrm{cr}} + \sqrt{(M_{\mathrm{s}} + W_{\mathrm{b}} f_{\mathrm{m}} + (W_{\mathrm{b}} f_{\mathrm{m}} a + v_0) N_{\mathrm{cr}})^2 - 4 W_{\mathrm{b}} f_{\mathrm{m}} a (W_{\mathrm{b}} f_{\mathrm{m}} + M_{\mathrm{s}}) N_{\mathrm{cr}}}}{2 W_{\mathrm{b}} f_{\mathrm{m}} a} \tag{8}$$

where a=1/$A_{\mathrm{b}} f_{\mathrm{c}}$.

3.3.3. Stability coefficient

The stability coefficient φ can be calculated as $\varphi=N/(Af_{\mathrm{c}})=\sigma/f_{\mathrm{c}}$ and $N/N_{\mathrm{cr}}=\sigma/\sigma_{\mathrm{cr}}$. Using Eqs. (5) and (6), it is possible to get an equation including the stability coefficient as follows:

$$\varphi\left(1+\frac{f_{\mathrm{c}} v_0 A_{\mathrm{b}}}{W_{\mathrm{b}} f_{\mathrm{m}} (1-\varphi \frac{f_{\mathrm{c}}}{\sigma_{\mathrm{cr}}})}\right)-\frac{M_{\mathrm{s}}}{W_{\mathrm{b}} f_{\mathrm{m}}}-1.0=0 \tag{9}$$

Define $\varepsilon_0 = \frac{A_{\mathrm{b}} v_0}{W_{\mathrm{b}}}$ as the equivalent relative bending of the splice columns [25] where W/A is the core distance of the equivalent section. The relative slenderness ratio is set as $\lambda_{\mathrm{rel}} = \frac{\lambda}{\lambda_{f_{\mathrm{c}}}} = \sqrt{\frac{f_{\mathrm{c}}}{\sigma_{\mathrm{cr}}}}$, where $\lambda_{f_{\mathrm{c}}} = \pi\sqrt{\frac{\mathrm{E}}{f_{\mathrm{c}}}}$. Then Eq. (9) can be rewritten as follows：

$$\varphi^2 - \left[\left(1+\frac{M_{\mathrm{s}}}{f_{\mathrm{m}} W_{\mathrm{b}}}\right)+\frac{1}{\lambda_{\mathrm{rel}}^{\ 2}}\left(1+\frac{f_{\mathrm{c}}\varepsilon_0}{f_{\mathrm{m}}}\right)\right]\varphi - \left(\frac{M_{\mathrm{s}}}{f_{\mathrm{m}} W_{\mathrm{b}}}+1\right)\frac{1}{\lambda_{\mathrm{rel}}^{\ 2}}=0 \tag{10}$$

The solution of Eq. (10) can be written as：

$$\varphi=\frac{\left(1+\frac{M_{\mathrm{s}}}{f_{\mathrm{m}}W_{\mathrm{b}}}\right)+\frac{1}{\lambda_{\mathrm{rel}}^{2}}\left(1+\frac{f_{\mathrm{c}}\varepsilon_{0}}{f_{\mathrm{m}}}\right)}{2}-\sqrt{\left[\frac{\left(1+\frac{M_{\mathrm{s}}}{f_{\mathrm{m}}W_{\mathrm{b}}}\right)+\frac{1}{\lambda_{\mathrm{rel}}^{2}}\left(1+\frac{f_{\mathrm{c}}\varepsilon_{0}}{f_{\mathrm{m}}}\right)}{2}\right]^{2}-\frac{1}{\lambda_{\mathrm{rel}}^{2}}\left(1+\frac{M_{\mathrm{s}}}{f_{\mathrm{m}}W_{\mathrm{b}}}\right)} \qquad (11)$$

where $\varepsilon_0 = \frac{A_{\mathrm{b}} v_0}{W_{\mathrm{b}}}$.

The form of this formula is similar to the prototype regarding the stability formula of the intact column in the American code NDS-1997 [26] and European code Eurocode 5-2000 [27]. In the proposed formula, the moment resistance ($\frac{M_{\mathrm{s}}}{f_{\mathrm{m}}W_{\mathrm{b}}}$) of the steel jacket to the joint is considered. Since the flexural section modulus of the semi-circular tenon is 0.5 times of the intact column, the value of the equivalent relative bending of the spliced columns increases and needs to be calculated correspondingly.

4. Finite element analysis

The distribution of the contact stress between the steel jacket and the splice joint is necessary to be determined before calculating the M_{s} in the theoretical analysis model (Eq. (2)). In this study, the stress distribution of the splice joint will be analyzed through numerical simulation. First, the finite element (FE) models of the splice columns are constructed in ABAQUS. The experimental data of the material property and the specimens are then used to verify the numerical model. The verified numerical model is subsequently used to analyze the buckling modes of the splice columns, the stress distribution of splice joints, and the effect of splice parameters on axial compressive strength.

4.1. Finite element model

4.1.1. Constitutive model of wood

The 8-node hexahedral linear-reduced integral element C3D8 with high accurate displacement calculation and high distortion tolerance is used to simulate the specimens [28]. It is well known that it is hard to accurately capture the mechanical behavior of the wood due to their complex constitutive relation under different loading conditions, such as the tensile brittle failure, compressive plastic property, and the different tensile and compressive strength in the same orientation. Here, the properties of the wood are defined by a combination of two methods to describe their mechanical behavior, namely Engineering Constants with Hill plasticity criterion and a user-defined material subroutine (VUMAT) in ABAQUS. In the former method, the Hill plasticity criterion is adopted to simulate the plastic stage of the wood [29, 30]. The local column coordinates are established to define the material properties of the columns (Fig. 6). In the latter method, the Yamada-Sun yield criterion is used to consider the interaction of multiple stress variables and the material failure mode. In the failure mode, the complex tensile and compressive anisotropy of wood is simplified as the three-fold model (Fig. 7) [31, 32]. The local rectangular coordinate is established to define the material properties of the column member and the longitudinal direction of the column is along the wood grain. In Fig. 7, X_t, Y_t, and Z_t denoted the tensile strength of the wood in longitudinal, transverse radial and transverse tangential directions, respectively. X_c, Y_c and Z_c denote the compressive strength of the wood in longitudinal, transverse radial and transverse tangential directions, respectively. The damage variable in three directions is defined to indicate the degree of damage. The element is considered as failed if the value of the damage variable goes beyond the threshold [31, 32].

The two afore-mentioned material description methods each have advantages and disadvantages. The advantages of the first method are as follows: 1) the plastic deformation of the wood under compression can be described; 2) the element will not fail under highly concentrated stress. The disadvantages are: 1) the tensile strength and compressive strength are the same in the same direction; 2) the brittle fracture in tension cannot be realistically represented. The advantages of VUMAT are: 1) the orthotropic strain-stress relationship can be well simulated in the elastic phase; 2) using the elastic strain energy, the tensile damage in three directions can be simulated effectively; 3) the compressive failure in grain can be simulated with the damage factor. The disadvantages are: 1) the model calculation is prone to be terminated when the elements fail under concentrated stress; 2) the strengthening effect of the compression strength in the transverse direction is not considered.

Considering the characteristics of the two material description methods, the VUMAT is used only in the timber splice joint. The method with Engineering Constants with Hill plasticity criterion is mainly used in the main column, especially the part with local extrusion from the edge of the steel jacket. The material properties in the model are determined according to the test data. The material properties of the model are listed in Table 4. The yield points and plasticity strength coefficients are listed in Table 5.

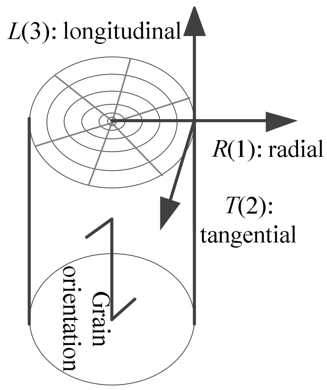

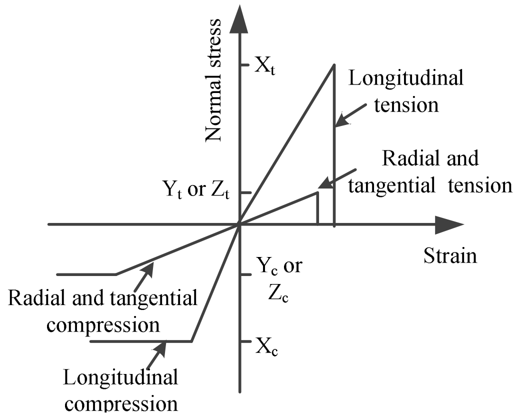

Fig. 6. System of principal axes in FE **Fig. 7.** Simplified constitutive model of wood in VUMAT

Table 4 Material property of the wood and steel jacket

	Orientation	Wood	Steel
Elastic modulus (MPa)	E_1	736.4	210000
	E_2	519.63	210000
	E_3	9700	210000
Poisson's ratio	v_{12}	0.683	0.3
	v_{13}	0.038	0.3
	v_{23}	0.034	0.3

Shear modulus (MPa)	G_{12}	237.84	—
	G_{13}	1272.8	—
	G_{23}	617	—
Density (g/cm^3)	ρ	0.385	7.8

Table 5 Yield points and plasticity strength coefficients assumed for analysis

Yield points (MPa)	σ_{11}	σ_{22}	σ_{33}	σ_{12}	σ_{13}	σ_{23}	σ^0
	3.2	3.2	29	4.47	8.95	8.95	29
Plasticity strength coefficients	R_{11}	R_{22}	R_{33}	R_{12}	R_{13}	R_{23}	
	0.11	0.11	1.0	0.27	0.53	0.53	

4.1.2. Contact model

The interaction between the components of the splice columns is modeled as "hard contact" in the normal direction. The "static-kinetic exponential decay" is used to model the relation between the tangential (friction) force and the relative sliding in the tangential direction [33]. The values of parameters in this friction model are listed in Table 6 [22, 34]. For the friction, the difference in the coefficient of friction in the longitudinal and transverse directions is not considered, and an average value in the two directions is used.

4.1.3. Boundary condition and solution

To model the hinged supports at the ends of the column, two reference points tied to the upper and lower end faces of the column are defined to model the hinge condition. The reference point at the base of the column is restrained in all three translational directions. The top reference point is restrained in two horizontal directions and load is applied by the vertical displacement.

The ABAQUS/Explicit solution module is used for quasi-static analysis. Generally, a static loading may be achieved by a sufficiently long loading duration. However, a long loading duration in Explicit analysis is computationally costly. To control computational cost with the Explicit approach, the mass scaling technique was employed which helps increase the time step in the Explicit calculation [35]. Furthermore, a energy criterion (kinetic energy of the model not exceeding 5-10% of the internal energy) was used to ensure a reliable and stable solution.

The meshed model of the spliced column is shown in Fig.8.

Table 6 Static and dynamic friction coefficient

Interaction	μ_s	μ_k	d_c
Wood-wood	0.332	0.262	3
Steel-wood	0.237	0.201	3

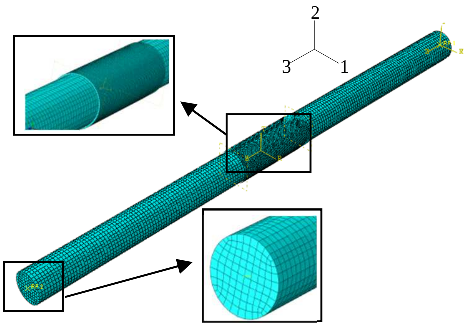

Fig. 8. The meshed model of the splice column

4.2. Validation of the finite element model

The finite element model described in section 4.1 is verified firstly by simulating the stress-strain behavior of the small wood samples and comparing the results with the data from the literature [36]. The whole FE model is then verified by simulating the experimental intact and spliced columns.

Following the work of [36], Khelifa et al. have conducted an experimental test on the longitudinal compressive behavior of small specimens. More details of the test are available in [36]. The numerical analysis of the small wood samples is conducted in this study. The associated results are compared with test data measured from Khelifa et al. [36]. The test and numerical results of strain versus stress are depicted in Fig. 9. The numerical results match well within the experimental results for the longitudinal compressive behavior.

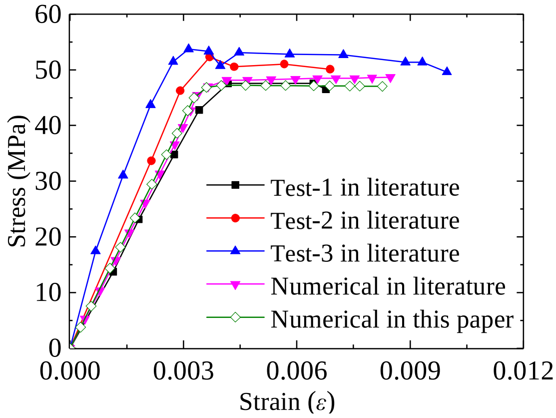

Fig. 9. The comparison of stress-strain of wood in simulation

Fig. 10 shows comparisons between the simulation and the test results for column specimens RC and SC3-2. For the intact column RC, the axial compression capacity of the column obtained from the FE simulation is smaller than that from the experiment with a relative error of about 20%. The numerical lateral stiffness agrees well with the test results. For the splice column (Fig. 10b), the FE simulated results agree well with the test results, both in terms of the axial compression capacity and the load-lateral displacement behavior. Overall, the FE model is capable of capturing the response of the columns robustly and the model can be used to analyze the influence of the key parameters, including L_e and L_t, on stiffness and strength of the spliced columns.

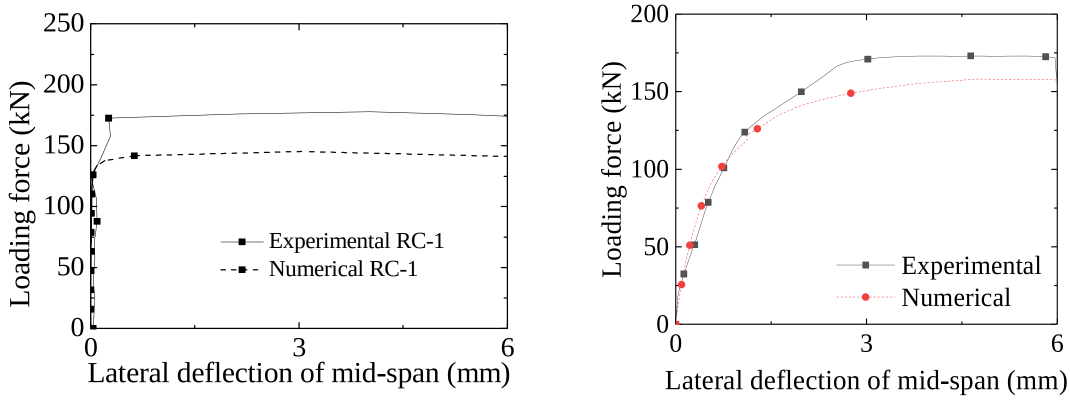

(a) RC-1 (b) SC3-2

Fig. 10. Comparisons between the simulation and test results in column specimens

A convergence analysis of the finite element model has been conducted to determine an appropriate mesh resolution. Five different mesh grid sizes have been examined using column SC2-2 as a sample specimen, with a total number of elements in the FE model being 0.46×10^4, 1.56×10^4, 2.42×10^4, 3.58×10^4, and 4.42×10^4, respectively. Fig.11 shows the variation of the computed loading capacity of the column with the reduction of the mesh grid size. It can be seen that when the number of elements is larger than 2.42×10^4, the mesh dimension has negligible influence on the loading capacity. Taking into account of the computational cost, the model with 2.42×10^4 elements is considered to be appropriate and is therefore used in this study. Within this mesh, the nominal element size for the steel jacket is approximately 4mm and that for the timber column is approximately 10mm.

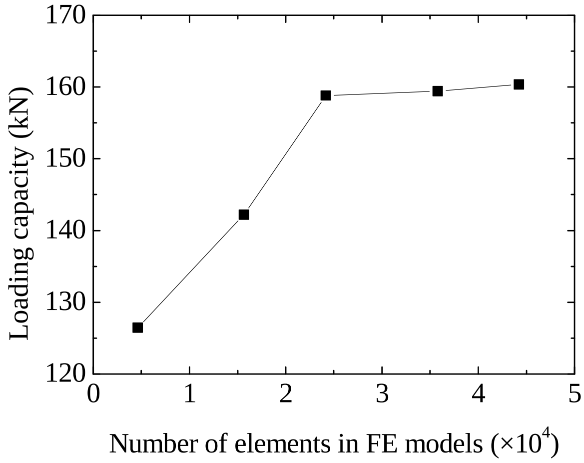

Fig. 11. **Convergence of finite element solution**

4.3. Buckling and modal analysis

In the finite element analysis for the axial capacity of the spliced columns, a linear buckling mode is employed to represent the influence of initial imperfections [37, 38]. Thus, a prior eigenvalue buckling analysis is needed, the result is then imported in proportion as the initial imperfection for the main analysis. Column SC2-1 is taken here as an example. The first three eigenmodes are shown in Fig. 12. Modes 1 and 2 are in correspondence with the bending modes III and I mentioned in Section 2.3, respectively. This tends to confirm that the main lateral bending direction of the splice columns is the bending III, followed by Type I. In the subsequent simulation, the first two eigenmodes are considered to represent the imperfection of the splice columns.

When Mode 1 is considered as initial imperfection, the lateral buckling section of the spliced columns exhibits type III. On the other hand, with Mode 2 imperfection, the lateral buckling direction of the spliced columns is inclined towards type I with a significant presence of type III. This is consistent with the observations from the experiment in that the lateral deformation of the spliced columns always had a significant component in the direction of type III. Hence, to simplify the model for the analysis of the effects of other parameters, Mode 1 is used as the initial imperfection in the subsequent simulations. Besides, based on trial comparisons between FE and the experimental results, a nominal deflection of 0.3‰ of the column length is adopted as the initial imperfection.

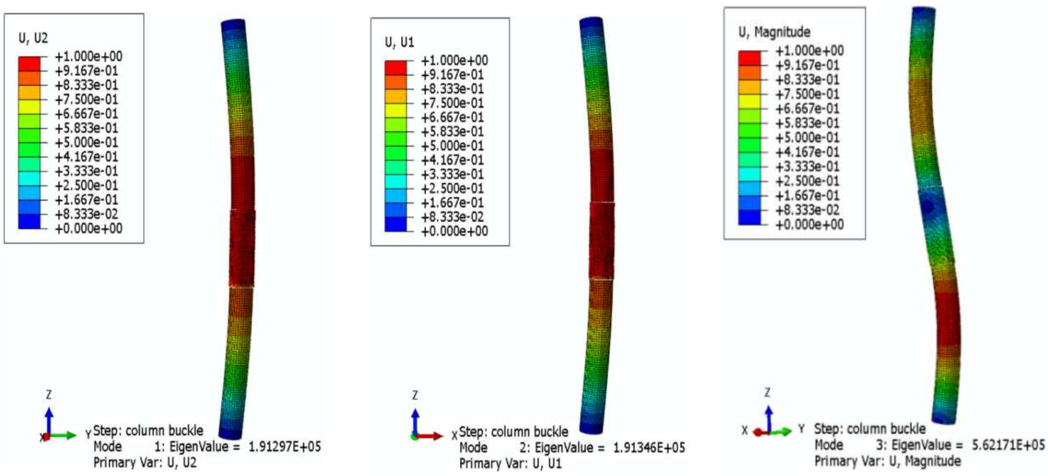

(a) (b) (c)

Fig. 12. The first three orders of eigenmodes of SC2-1: (a) Mode 1; (b) Mode 2; (c) Mode 3

4.4. Analysis of contact pressure on the steel jacket

The analysis in Section 4.3 shows that for the spliced columns the buckling Mode 1 and Mode 2 corresponds to the bending section modes of type III and I (see Section 2.4), respectively. It can be understood that when the steel jacket extension length (L_e) is small, the buckling Mode 2 will tend to develop due to the weakening of the section at the top and bottom of the splice. Otherwise Mode 1 will be the dominant buckling mode. This also implies that the interaction between the steel jacket beyond the splice joint has an important effect on the failure mode of the splice column.

Fig. 13 shows the contact pressure distribution of the splices columns. A stress concentration can be observed at the concave side contacting the upper edge of the steel jacket. The contact pressure on the concave side of the splice column gradually reduces from the upper edge of the steel jacket when the L_e is less than 100 mm. The contact pressure of the splice column at the upper edge of the steel jacket is maximum while it is minimum at the splicing seam. When L_e in increased to 150mm, the contact pressure of the splice column at the upper edge of the steel jacket is reduced and the pressure in the splicing seam is increased. The contact pressure distribution in the convex side is contrary to the distribution in the concave side.

To further understand the contact stress distribution between the steel jacket and the timber splice joint, three paths are selected to analyze the node pressure. Path 1 (Fig. 14a) is the contact path between the concave side of the spliced column and the upper edge of the steel jacket. Path 2 (Fig. 14b) is the vertical contact path on the concave side of the spliced column from the splicing seam to the upper edge of the steel jacket. Path 3 (Fig. 14c) is the vertical contact path in the convex side of the splice column from the splicing seam to the upper edge of the steel jacket.

The contact pressure of the nodes in each path is shown in Fig.15. The change of contact pressure in Path 1 indicates that the contact stress reduces along the arc from the mid-point to the ends, similar to a sinusoidal distribution (Fig. 15a). The contact pressure in Path 2 indicates that the contact pressure increases from the point with a distance of (L_e/3) mm to the upper edge of the steel jacket (Fig. 15b). The maximum pressure is on the order of 5 MPa at the upper edge of the steel jacket due to the stress concentration. Hence, the wood in the upper edge has yielded in the transverse direction. The stress at the beginning ($2L_e$/3) mm of the Path 2 is about 0.5 times of the stress at the upper edge of the steel jacket. The contact pressure in Path 3 indicates that the contact pressure in the convex side increases with the length of L_e when L_e increases from 30mm to 100mm (Fig. 15c). Fig. 13a shows that the maximum value of the contact pressure is linearly related to L_e. Based on the regression analysis, the contact pressure is approximately (L_e/32) MPa.

The length of the contact pressure distribution is about (L_e-20) mm showed in Fig. 16b. The pressure in the first 2/3rds of the distribution length approaches the maximum pressure. Then, the pressure in the last 1/3rd of the distribution length decreases to zero gradually. During the increase of the length of the steel jacket from 100mm to 150mm, the contact pressure is along the entire length of the Path 3. The pressure in the first 2/3L_e is even and approaches 0.5 times of the compressive strength in the radial direction. The pressure in the last 1/3L_e decreases to zero gradually.

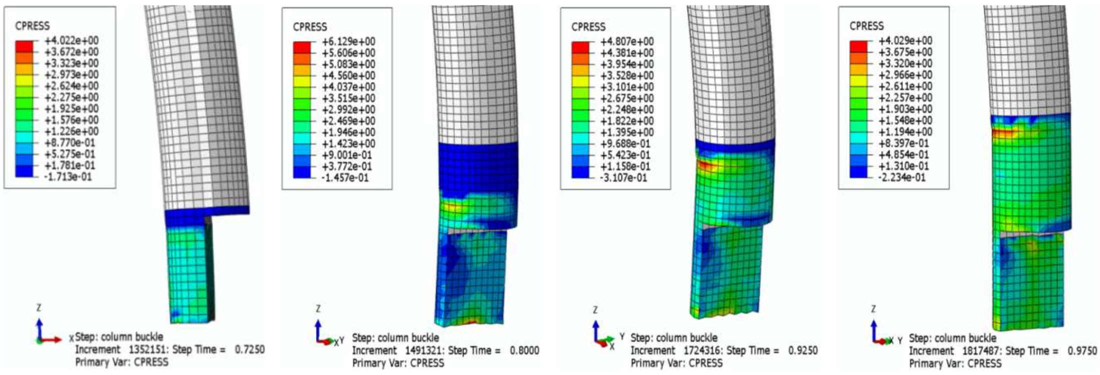

(a) (b) (c) (d)

Fig. 13. Contact pressure distribution of the splice joint under the peak loading (L_t=130mm): (a) L_e=0mm; (b) L_e=50mm; (c) L_e=100mm; (d) L_e=150mm

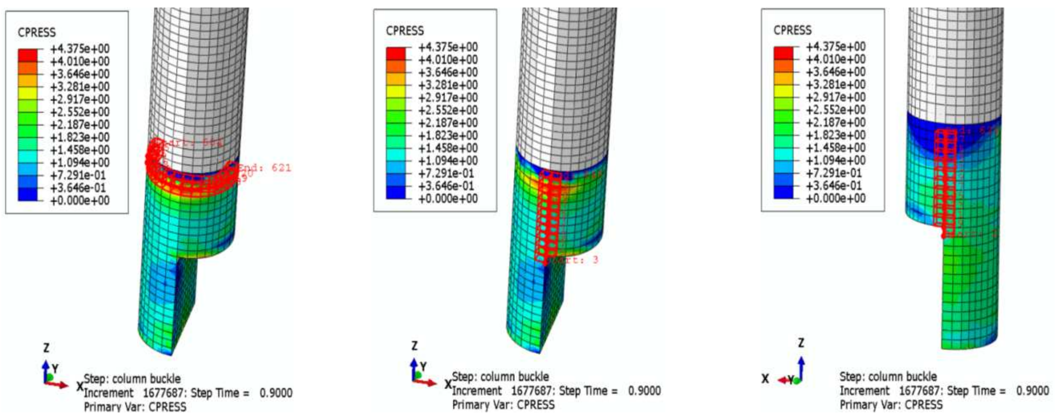

(a) (b) (c)

Fig. 14. Contact pressure path 1-3: (a) Path 1; (b) Path 2; (c) Path 3

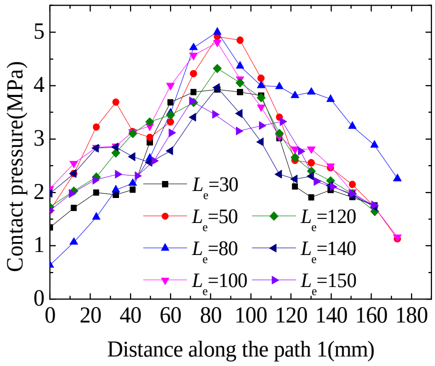

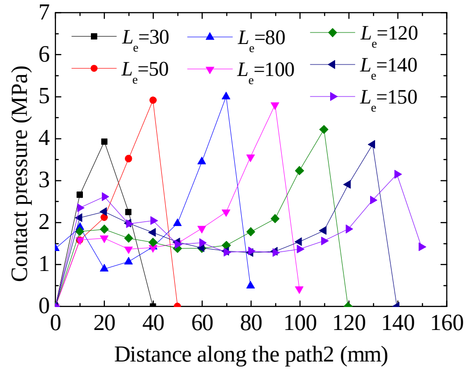

(a) (b)

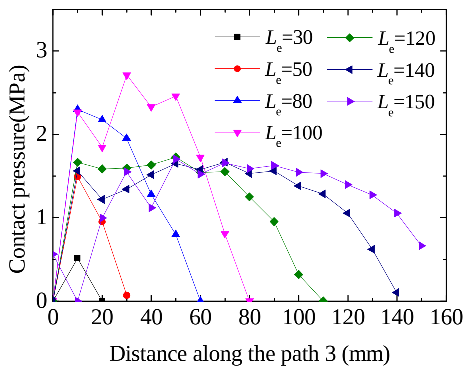

(c)

Fig. 15. Contact pressure in the path 1-3 under the peak loading (L_t=130mm, L_e=30~150mm): (a) Path 1; (b) Path 2; (c) Path 3

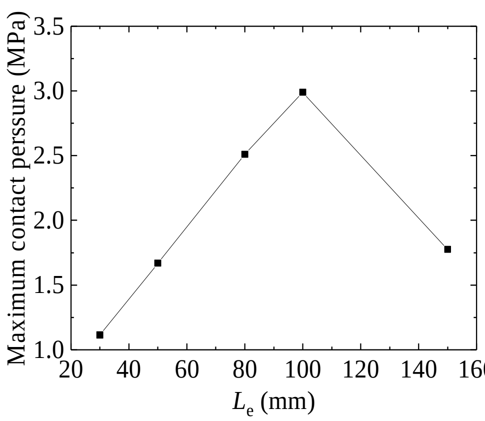

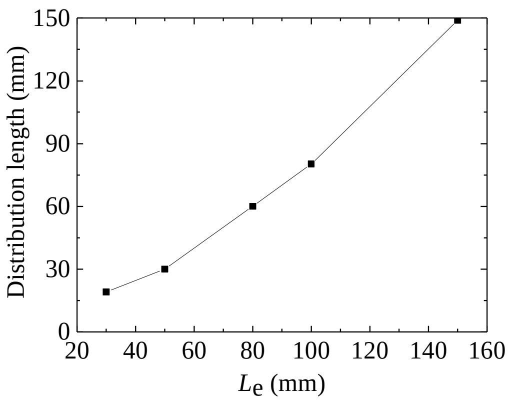

(a) (b)

Fig. 16. Trends of the contact pressure distribution in Path 3: (a) Maximum contact pressure; (b) Length of the contact pressure distribution

Considering L_e and L_t as parameters (Fig. 17 (a)), the bearing capacity indicates that increasing L_e generally enhances the capacity when L_e varies in the range of 80mm~150mm. However, the excessive length of the steel jacket can be harmful to the behavior of the spliced columns since the large difference of stiffness between the steel jacket and the joint usually causes stress concentration in the joint. From the apparent increase of the stiffness and bearing capacity with $L_e \geq 50$mm, the recommended range of L_e is 0.5~1.5 times of the column diameter. Therefore, a reasonable length of the steel jacket may be set to 2~4.5 times of the column diameter. Fig. 17(b) illustrates the interaction effect between L_s and L_t on the bearing capacity. A similar trending with Fig. 17(a) can be observed that both L_s and L_t have a positive impact on the bearing capacity.

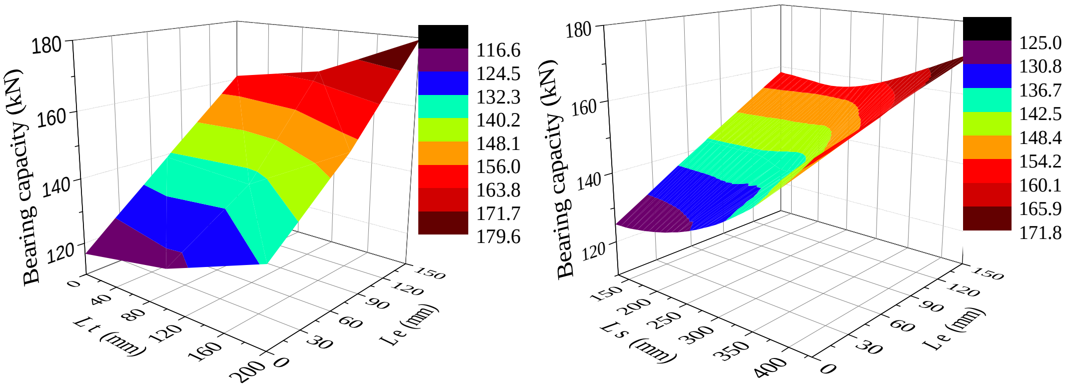

(a) (b)

Fig. 17. Influence of parameters on the bearing capacity of a splice column: (a) L_t and L_e; (b) L_s and L_e

4.5. Moment resistance induced by the steel jacket

Based on the theoretical and numerical analysis, a free body diagram of forces for the upper-half of the timber column is shown in Fig. 18. In Fig. 18a, σ_{a1}, and σ_{a2} denote the maximum contact pressure at the beginning ($2L_e/3$) and the last ($L_e/3$) of Path 2, respectively. The distribution along the inner face of the steel jacket in the circumferential direction is simplified in Fig.14c and the contact pressure on the concave side can be expressed as $\sigma_{ai\theta}$=($\sigma_{ai}\sin\theta$), where θ is the angle as shown in Fig. 18c. σ_{a1} and σ_{a2} are local compressive strength in the radial direction and according to the numerical analysis they may be assumed as 0.5 times of the local compressive strength, respectively, i.e. σ_{a1}=$f'_{c,R}$ = 2σ_{a2}. σ_t was the maximum contact pressure in the convex side of the splice column of the Path 3. Based on the numerical results, (L_e/32) MPa is adopted as the value of σ_t when L_e is in the range of 30 mm to 100 mm. When L_e is in the range of 100 mm to 150 mm (Fig. 18b), σ_t is taken equal to 0.5 times of the compressive strength in the radial direction, i.e. σ_t=$f_{c,R}$/2.

F_{a1} and F_{a2} are the components of the contact force on the concave side induced by the steel jacket (horizontal to the right in the diagram). F_t is the component along the direction of the lateral deflection of the spliced columns of the contact force on the convex side induced by the steel jacket (horizontal to the left in the diagram). f_{a1} and f_{a2} are the vertical friction on the concave side induced by the steel jacket. f_{t1} and f_{t2} are the vertical friction on the concave side induced by the steel jacket. M is the bending moment in the middle section of the column with initial bending (caused by initial defects) under the peak load (N= peak load P); M_1 is the bending moment at the middle section of the column carried by the wooden tenon at the upper splicing section. The circumferential contact pressure distribution along the inner side of the steel jacket is simplified in Fig.18c and the contact pressure with random degree in convex side can be expressed as $\sigma_{t\theta}$=($\sigma_t\sin\theta$).

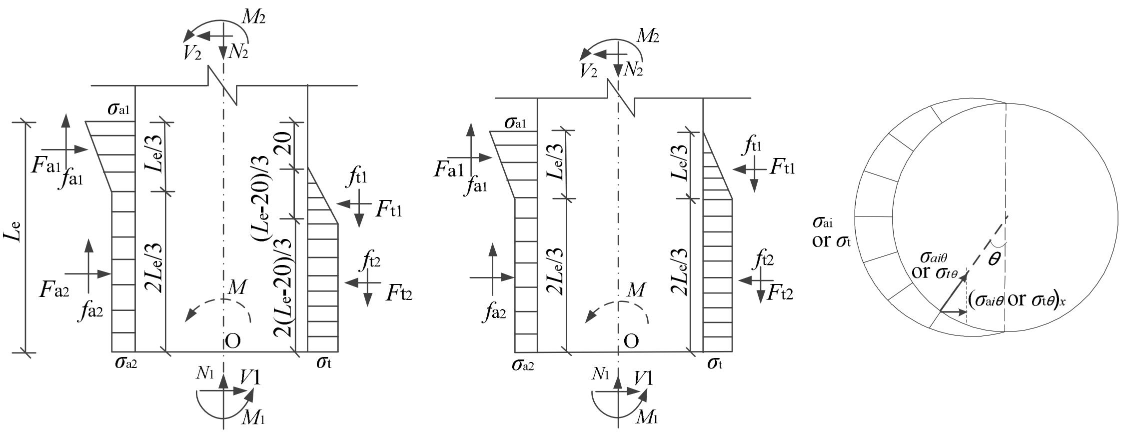

(a) (b) (c)

Fig. 18. Free body diagraph of upper-half splice comun under peak load: (a) Elevation view ($30 \le L_e \le 100$); (b) Elevation view ($100 < L_e \le 150$); (c) Top view

Based on the finite element analysis results, $\sigma_{a1}=f'_{c,R}=2\sigma_{a2}$ and $\sigma_{ai\theta}=(\sigma_{ai}\sin\theta)$, the effect on the splice column generated by contact pressure($\sigma_{ai\theta}$) and friction (f_a) in the concave side can be calculated as follows：

$$F_{a1}=\frac{L_e}{3}\int_0^{\pi}(\frac{f'_{c,R}}{2})(\sin\theta)^2\,rd\theta+\frac{1}{2}(\frac{L_e}{3})\int_0^{\pi}(\frac{f'_{c,R}}{2})(\sin\theta)^2\,rd\theta=\frac{\pi}{8}f'_{c,R}L_e r \tag{12}$$

$$M_{a1}=\left(\frac{L_e}{3}\int_0^{\pi}(\frac{f'_{c,R}}{2})(\sin\theta)^2\,rd\theta\right)\left(\frac{2}{3}L_e+\frac{L_e}{3}\frac{1}{2}\right)+\left(\frac{1}{2}(\frac{L_e}{3})\int_0^{\pi}(\frac{f'_{c,R}}{2})(\sin\theta)^2\,rd\theta\right)\left(\frac{2L_e}{3}\frac{1}{2}\right)=\frac{23\pi}{216}f'_{c,R}L_e^{\,2}r \tag{13}$$

$$F_{a2}=\frac{2L_e}{3}\int_0^{\pi}(\frac{f'_{c,R}}{2})(\sin\theta)^2\,rd\theta=\frac{\pi}{6}f'_{c,R}L_e r \tag{14}$$

$$M_{a2}=F_{a2}\left(\frac{2L_e}{3}\frac{1}{2}\right)=\frac{\pi}{18}f'_{c,R}L_e^{\,2}r \tag{15}$$

$$M_{sa}=M_{a1}+M_{a2}=\frac{35\pi}{216}f'_{c,R}L_e^{\,2}r \tag{16}$$

$$f_{a1}+f_{a2}=\left(\frac{L_e}{3}\int_0^{\pi}(\frac{f'_{c,R}}{2}\mu\sin\theta)rd\theta\right)+\left(\frac{1}{2}(\frac{L_e}{3})\int_0^{\pi}(\frac{f'_{c,R}}{2}\mu\sin\theta)rd\theta\right)=\frac{7}{6}f'_{c,R}L_e r\mu \tag{17}$$

$$M_{saf}=\left(L_e\int_0^{\pi}(\frac{f'_{c,R}}{2}\mu\sin\theta)(r\sin\theta)\,rd\theta\right)+\left(\frac{1}{2}(\frac{L_e}{3})\int_0^{\pi}(\frac{f'_{c,R}}{2}\mu\sin\theta)(r\sin\theta)\,rd\theta\right)=\frac{7\pi}{24}f'_{c,R}L_e r^2\mu \tag{18}$$

where r denotes the radius of the splice column; $f'_{c,R}$ denotes the local compressive strength in the radial direction.

For L_e ranging from 30mm to 100mm, $\sigma_t=(L_e/32)$MPa and $\sigma_{t\theta}=(\sigma_t\sin\theta)$. The effect on the joint of the spliced columns generated by steel jacket at the concave side can be calculated as follows：

$$F_{\mathrm{t1}}=\frac{1}{2}\frac{(L_{\mathrm{e}}-20)}{3}\int_{0}^{\pi}(\frac{L_{\mathrm{e}}}{32})(\sin\theta)^{2}\,rd\theta=\frac{\pi}{384}(L_{\mathrm{e}}-20)L_{\mathrm{e}}r \tag{19}$$

$$F_{\mathrm{t2}}=\frac{2(L_{\mathrm{e}}-20)}{3}\int_{0}^{\pi}(\frac{L_{\mathrm{e}}}{32})(\sin\theta)^{2}\,rd\theta=\frac{\pi}{96}(L_{\mathrm{e}}-20)L_{\mathrm{e}}r \tag{20}$$

$$M_{\mathrm{st}}=F_{\mathrm{t1}}\left(\frac{2(L_{\mathrm{e}}-20)}{3}+\frac{(L_{\mathrm{e}}-20)}{3}\frac{1}{3}\right)+F_{\mathrm{t2}}\left(\frac{2(L_{\mathrm{e}}-20)}{3}\frac{1}{2}\right)=\frac{5\pi}{1728}L_{\mathrm{e}}(L_{\mathrm{e}}-20)^{2}r \tag{21}$$

$$\begin{aligned}M_{\mathrm{stf}}&=\left(\frac{1}{2}\frac{(L_{\mathrm{e}}-20)}{3}\int_{0}^{\pi}(\frac{L_{\mathrm{e}}}{32}\mu\sin\theta)(r\sin\theta)rd\theta\right)+\left(\frac{2(L_{\mathrm{e}}-20)}{3}\int_{0}^{\pi}(\frac{L_{\mathrm{e}}}{32}\mu\sin\theta)(r\sin\theta)rd\theta\right)\\&=\frac{5\pi}{384}L_{\mathrm{e}}(L_{\mathrm{e}}-20)r\mu\end{aligned} \tag{22}$$

Substituting Eqs. (12)~(22) into Eq. (2), the moment resistance induced by the steel jacket for the splicing column can be expressed as:

$$M_{\mathrm{s}}=-\frac{5\pi}{1728}L_{\mathrm{e}}(L_{\mathrm{e}}-20)^{2}r+\frac{35\pi}{216}f_{\mathrm{c,R}}^{'}L_{\mathrm{e}}^{2}r+\frac{5\pi}{384}L_{\mathrm{e}}(L_{\mathrm{e}}-20)r\mu+\frac{7\pi}{24}f_{\mathrm{c,R}}^{'}L_{\mathrm{e}}r^{2}\mu \tag{23}$$

For L_{e} ranging from 100mm to 150mm, $\sigma_{\mathrm{t}}=f_{\mathrm{c,R}}/2$ and $\sigma_{\mathrm{t}\theta}=(\sigma_{\mathrm{t}}\sin\theta)$. Thus,

$$F_{\mathrm{t1}}=\frac{1}{2}\frac{L_{\mathrm{e}}}{3}\int_{0}^{\pi}(\frac{f_{\mathrm{c,R}}}{2})(\sin\theta)^{2}\,rd\theta=\frac{\pi}{24}f_{\mathrm{c,R}}L_{\mathrm{e}}r \tag{24}$$

$$F_{\mathrm{t2}}=\frac{2L_{\mathrm{e}}}{3}\int_{0}^{\pi}\frac{f_{\mathrm{c,R}}}{2}(\sin\theta)^{2}\,rd\theta=\frac{\pi}{6}f_{\mathrm{c,R}}L_{\mathrm{e}}r \tag{25}$$

$$M_{\mathrm{st}}=F_{\mathrm{t1}}\left(\frac{2L_{\mathrm{e}}}{3}+\frac{L_{\mathrm{e}}}{3}\frac{1}{3}\right)+F_{\mathrm{t2}}\left(\frac{2L_{\mathrm{e}}}{3}\frac{1}{2}\right)=\frac{19\pi}{216}f_{\mathrm{c,R}}L_{\mathrm{e}}^{2}r \tag{26}$$

$$M_{\mathrm{stf}}=\left(\frac{1}{2}\frac{L_{\mathrm{e}}}{3}\int_{0}^{\pi}(\frac{f_{\mathrm{c,R}}}{2}\mu\sin\theta)(r\sin\theta)rd\theta\right)+\left(\frac{2L_{\mathrm{e}}}{3}\int_{0}^{\pi}(\frac{f_{\mathrm{c,R}}}{2}\mu\sin\theta)(r\sin\theta)rd\theta\right)=\frac{5\pi}{24}f_{\mathrm{c,R}}L_{\mathrm{e}}r\mu \tag{27}$$

Substituting Eqs. (12)~(18) and Eqs. (24)~(27) into Eq. (2), the moment resistance induced by the steel jacket for the splice column could be calculated as:

$$M_{\mathrm{s}}=-\frac{19\pi}{216}f_{\mathrm{c,R}}L_{\mathrm{e}}^{2}r+\frac{35\pi}{216}f_{\mathrm{c,R}}^{'}L_{\mathrm{e}}^{2}r+\frac{5\pi}{24}f_{\mathrm{c,R}}L_{\mathrm{e}}r\mu+\frac{7\pi}{24}f_{\mathrm{c,R}}^{'}L_{\mathrm{e}}r^{2}\mu \tag{28}$$

When the length of steel jacket ranges from 0 mm to 30 mm, a conservative calculation may be carried out by assuming no steel jacket effect at the top (or bottom) section of the spliced joint, and hence the moment resistance is governed by the bending resistance of the half column section in the weaker direction (perpendicular to the splice face).

5. Validation of the theoretical model

The applicability of the theoretical model is validated by comparing with the experimental and numerical results considering various parameters, such as L_e, tree species, column length, and diameter of the splice columns.

5.1. Experimental bearing capacity

The buckling section mode III corresponding to the buckling Mode 1 is assumed in the calculations. A comparison of the bearing capacities obtained using a) the proposed bearing capacity formula, b) the stability coefficient method, c) FE analysis, and d) the experiment, are shown in Fig. 19. SC1-1 does appear to be unsafe and SC3-2 is over conservative. But it should be noted that specimen SC1-1 had apparent initial bending in the experiment (Section 2.3), and this led to a larger lateral deflection before the ultimate load and an eccentric compression failure. Therefore, the test loading capacity of the SC1-1 was smaller than its real capacity if there was not the initial bending, and the comparison with the result from the theoretical model would be better if the real bending capacity of the specimen was obtained more accurately. For specimen SC3-2, the two splice parts wrapped in the steel jacket did not contact each other at the beginning of the test. This means that the actual length of the SC3-2 was shorter than other specimens, and this explains at least in part as why the test loading capacity of the SC3-2 was higher than the result from the theoretical mode. Except for SC1-1 and CS3-2, the calculated results compared favourably with experimental results, with both the bearing capacity formula and the stability coefficient method achieving an average error at about 15%. When the bearing capacity formula and the stability coefficient method were used to calculate the bearing capacity, the average relative error between the calculated and the finite element results are 7.7% and 11.9%, respectively.

5.2. *Influence of L_e on the bearing capacity*

The bearing capacity calculated from the bearing capacity formula and the stability coefficient is compared with the bearing capacity from the FE simulation considering L_e as the parameter. (P_u/P_{u0}) is defined to describe the ratio of the ultimate loading of the splice columns to that of the intact column. Fig. 20 shows the relation between L_e and (P_u/P_{u0}) in the FE simulation and the theoretical results. The relative error between the results calculated from the bearing capacity formula and by the FE simulation is less than 11% when the L_e ranged from 30mm to 100mm. The relative error between the results from the stability coefficient method and the FE simulation is less than 12%. When the L_e ranges from 100mm to 150mm, the relative errors are less than 10% and 21%, respectively, from using the bearing capacity formula and the stability coefficient as compared with the FE results.

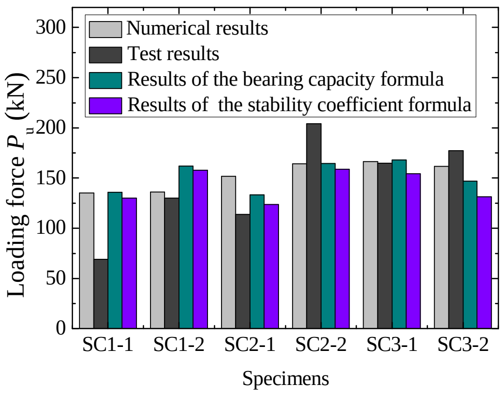

Fig.19. Comparison of test and theoretical results

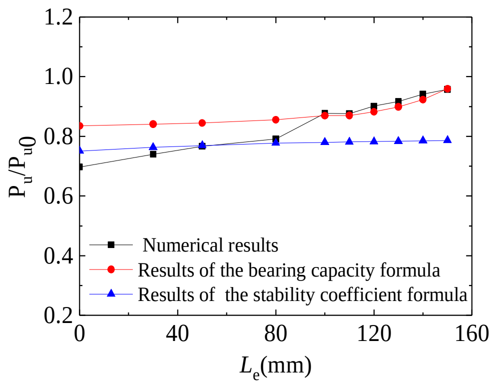

Fig. 20. Relations of L_e vs P_u/P_{u0}

5.3. *Influence of tree species on the bearing capacity*

Korean pine, Betula and Douglas fir are chosen as the tree species of the splice columns [22, 23, 31, 39], and the splice parameters and dimensions are set the same as test specimen SC2. The comparisons show that the relative errors in the calculated bearing capacity using the bearing capacity formula and using the stability coefficient are less than 13% and 6%, respectively, as compared with the FE simulation results.

5.4. Influence of length of spliced columns on the bearing capacity

The bearing capacity of the spliced columns having the same splice parameters as SC2 but with a varying column length are calculated by the theoretical formulas in comparison with the FE simulation results. The representative column lengths of 1400mm, 2200mm, and 2600mm, are considered. The initial bending imperfection of each column is set in proportion to the column length. The relative errors using the bearing capacity formula and the stability coefficient are less than 21% and 11%, respectively, as compared to the FE simulation results.

6. Application considerations

6.1. The splice position

The proposed bearing capacity calculation formula has been developed on the assumption that the splice takes place at the middle of the column. The actual position of the splice joint at different positions along the height of the column will affect the bearing capacity. To investigate such an effect, three different splice heights (i.e. $1/5l$, $1/4l$, and $1/3l$) from the bottom of the column are examined using finite element simulation. The results are shown in Fig. 21. The column with the splice at $1/5l$ height actually failed at mid-span similar to the intact columns. The failure of the columns with the splice at $1/4l$ and $1/3l$ height happened at the splice joints. Their bearing capacities are between that of the intact column and that of the spliced column with the splice joint at mid-span but are closer to the latter. Therefore for simplification, it is recommended that the capacity of the intact column be used for a spliced column with the splice height within $1/5l$ from the column bottom, whereas for columns with the splice at the height ranging from 1/5*l* to 1/2*l*, the calculation model of the spliced column with the splice joint at mid-span is used to be conservative.

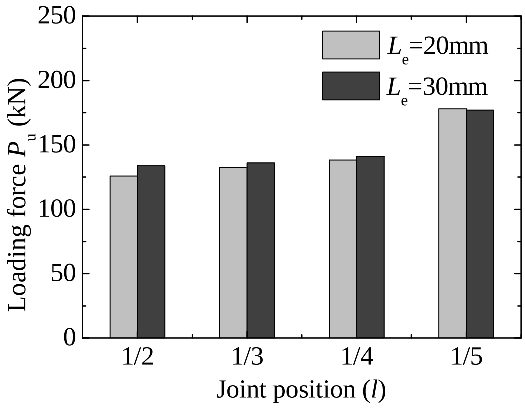

Fig.21. Joint position vs loading force

6.2. Spliced columns with different timber materials

In actual applications, the columns being splice-retrofitted may contain different materials (or material properties) on the two sides of the splice. In such cases, it is suggested that the weaker material property of the two parts be used in applying the proposed analytical formula to calculate the bearing capacity of the spliced column.

7. Conclusions

In this paper, an analytical model has been proposed for the calculation of the axial compressive strength and the stability coefficient for spliced columns retrofitted with the steel jacket. To assist in the formulation of the analytical model, a detailed finite element model is developed, which is then used to analyze the bending and buckling modes of the spliced columns and the contact stress within the splice joint. The theoretical model has been verified by comparing with the experimental data and the FE simulation results with varying design parameters, including the jacket extension length L_e, tree species, and column length. The following conclusions may be drawn:

(1) The proposed analytical model is capable of predicting the bearing capacity of the spliced

columns retrofitted with the steel jacket with good accuracy.

(2) A reasonable splice length can ensure a reliable connection of the splice joint while avoiding negative effects due to incompatible stiffness with the column section. For the spliced columns covered in this study, the length of the splice (L_e) and the total length of the steel jacket (L_s) are recommended to be in the range of 0.5~1.5 and 2~4.5 times of the column diameter, respectively.

(3) For columns with a spliced joint enhanced by a steel jacket, buckling mode 1 in the direction parallel to the splice face is generally a dominant mode of bending and failure, which corresponds to buckling section mode III. Buckling mode 2, which corresponds to buckling section type I (perpendicular to the splice face), could become important with a short jacket extension length.

(4) For columns with a splice position not at the mid-span, it is recommended that the same bearing capacity calculation formula as the mid-span splice case be applied if the splice position is between 1/5 and 1/2 of the column length from the column end. It is also reasonable to use the weaker material properties between the two splice parts in the calculation of the bearing capacity of a spliced column.

CRediT authorship contribution statement

Hongmin Li: Conceptualization, Methodology, Investigation, Software, Formal analysis, Writing - original draft, Writing - review & editing, Visualization, Funding acquisition. **Hongxing Qiu**: Conceptualization, Supervision, Funding acquisition. **Yong Lu**: Conceptualization, Supervision, Validation, Writing - review & editing.

Declaration of Competing Interest

The authors declare that they have no known competing financial interests or personal relationships that could have appeared to influence the work reported in this paper.

Acknowledgments

This work was financially supported by the Thirteenth Five-Year National Science and Technology Support Program (2017YFC0703503) of China, the Personal Scientific Research Start-up Funds (163020125) from NFU, and the National Science Foundation for Young Scientists of China (51908291).

References

[1] Dorn M, De Borst K, Eberhardsteiner J. Experiments on dowel-type timber connections. Eng Struct, 2013; 47(1): 67-80.

[2] Koch H, Eisenhut L, Seim W. Multi-mode failure of form-fitting timber connections–Experimental and numerical studies on the tapered tenon joint. Eng Struct, 2013; 48: 727−738.

[3] Caldeira T V P, Dourado N, De A M P, et al. Quasi-static behavior of moment-carrying steel–wood doweled joints. Constr Build Mater, 2014; 53: 439−447.

[4] Schoenmakers J C M D, Jorissen A J M. Failure mechanisms of dowel-type fastener connections perpendicular to grain. Eng Struct, 2011; 33(11): 3054−3063.

[5] Sangree RH, Schafer BW. Experimental and numerical analysis of a halved and tabled traditional timber scarf joint. Constr Build Mater 2009; 23 (2): 615-624.

[6] Arciszewska-Kędzior A, Kunecký J, Hasníková H, Sebera V. Lapped scarf joint with inclined faces and wooden dowels: Experimental and numerical analysis. Eng Struct 2015; (94): 1-8.

[7] Xu BH, Bouchaïr A, Racher P. Analytical study and finite element modelling of timber connections with glued-in rods in bending. Constr Build Mater 2012; 34: 337-345.

[8] Li HM, Lam F, Qiu HX. Comparison of glulam beam-to-beam connections with round dovetail and half-lap joints reinforced with self-tapping screws. Constr Build Mater 2019, 227: 116437.

[9] Gattesco N, Gubana A, Buttazzi M, Melotto M. Experimental investigation on the behavior of glued-in rod joints in timber beams subjected to monotonic and cyclic loading. Eng Struct 2017; 147: 372–84.

[10] Ogrizovic J, Wanninger F, Frangi A. Experimental and analytical analysis of moment-resisting connections with glued-in rods. Eng Struct 2017; 145: 322–32.

[11] Yang H, Liu W, Ren X. A component method for moment-resistant glulam beam–-column connections with glued-in steel rods. Eng Struct 2016; 115 :42–54.

[12] Cepelka M, Malo KA. Moment resisting splice of timber beams using long threaded rods and grout-filled couplers – experimental results and predictive models. Constr Build Mater 2017; 155: 560–70.

[13] Moment resisting on-site splice of large glulam elements by use of mechanically coupled long threaded rods. Eng Struct 2018; 163: 347–357.

[14] Xu QF. Experimental study of strengthening methods of partially-damaged circular wood columns. J Cent South Univ (Sci Tech), 2012; 43(4): 1506−1513. (in Chinese)

[15] Xu QF, Zhu L. An experimental study on partially-damaged wood columns repaired and strengthened with CFRP. China Civ Eng J, 2007; 40(8): 41−46. (in Chinese)

[16] Buchanan, A. H. (1984). Strength Model and Design Method for Bending and Axial Load Interaction in Timber Members, Ph.D. Thesis, University of British Columbia, Vancouver, Canada.

[17] Huang, Z., Chen, Z., Huang, D., Chui, Y., and Bian, Y. (2018). "An inelastic model for analyzing intermediately slender engineered bamboo/wood columns subjected to biaxial bending and compression," BioRes. 13(2), 2814-2833.

[18] Song, X., and Lam, F. (2009). “Laterally braced wood beam-columns subjected to biaxial eccentric loading,” Comput. Struct. 87(17-18), 1058-1066.

[19] Li HM, Qiu HX, Zhao Z, Lu Y. Experimental study on splice-jointed timber columns reinforced with steel jackets. J Cent South Univ (Sci Technol), 2018; 49(1): 192-200. (in Chinese)

[20] Li HM, Qiu HX, Zhao Z, Lu Y. Axial compression behaviour of retrofitted long timber columns. Adv Struct Eng, 2018; 21(3): 445-459..

[21] GB/T 1935−2009. Method of testing in compressive strength parallel to grain of wood. Beijing: China Standards Press; 2009. (in Chinese)

[22] Chen Z. Behaviour of typical joints and the structure of Yingxian wood pagoda. PhD Thesis, Harbin: Harbin Institute of Technology. School of Civil Engineering, 2011: 191−192. (in Chinese)

[23] Wang L, Lu Z, Shen SJ. Study on twelve elastic constant values of Betula platyphylla Suk. Wood. J Beijing For Univ, 2004; 25(6): 64−67.

[24] GB/T 228.1−2010, Metallic materials-Tensile testing-Part 1: Method of test at room temperature. Beijing: China Standards Press; 2011. (in Chinese)

[25] Pan J, Zhu E. Wood structure design principle. Beijing: China Architecture and Building Press; 2009. (in Chinese)

[26] NDS-1997, National Design Specification (NDS) for wood construction, Washington: American Forest and Paper Association; 1997.

[27] ENV 1995-1-1:2000 Eurocode 5 (2000) Design of timber structures, Part 1. Brussels: Comite Europeen de Normalisation; 2000.

[28] Chen C. Integral mechanics property analysis and safety evaluation of ancient timber structures. PhD Thesis, Nanjing: Southeast University. School of Civil Engineering, 2016: 36. (in Chinese)

[29] Hill R. The mathematical theory of plasticity. London: Oxford University Press, 1950.

[30] Nowak TP, Jasieńko J, Czepiżak D. Experimental tests and numerical analysis of historic bent timber elements reinforced with CFRP strips. Constr Build Mater, 2013; (40): 197-206.

[31] Li X. Numerical analysis of the fire resistance of post-beam timber frame. Master Thesis, Nanjing: Southeast University. School of Civil Engineering, 2014: 9-28. (in Chinese)

[32] Zhang J, Wang YX, Li LF, Xu QF. Thermo-mechanical behaviour of dovetail timber joints under fire exposure. Fire Safety J, 2017. (article in press)

[33] Chen C, Qiu H, Lu Y. Flexural behaviour of timber dovetail mortise–tenon joints. Constru Build Mater, 2016; 112: 366-377.

[34] Meng Q, The study for frictional properties of wooden materials and the impact on wood structure design. PhD Thesis, Harbin: Northeast Forestry University. School of Mechanical and Electrical Engineering, 2010: 34−36.

[35] Cao F, Shi Y. The FAQ solution for ABAQUS finite element analysis. Beijing: China Machine Press; 2009.

[36] Khelifa M, Loperena N, Bleron L, Khennane A. Analysis of CFRP-strengthened timber beams. J Adhes Sci Technol.2014; 28(1): 1-14. Khelifa M, Vila Loperena N, Bleron L,.

[37] Bisagni C. Numerical analysis and experimental correlation of composite shell buckling and post-buckling. Compos Part B: Eng, 2000; 31(8): 655-667.

[38] Priyadarsini RS, Kalyanaraman V, Srinivasan SM. Numerical and experimental study of buckling of advanced fiber composite cylinders under axial compression. Int J Struct Stab Dy, 2012; 12(04): 1250028.

[39] Long W. Wood structure design manual. Beijing: China Architecture and Building Press; 2005. (in Chinese)